Operando Fe Dissolution in Fe-N-C Electrocatalysts during Acidic Oxygen Reduction and Impact of Local pH Change

Angus Pedersen,[a,b,c‡] Kavita Kumar,[d‡] Yu-Ping Ku,[d,e] Vincent Martin,[c] Laetitia Dubau,[c] Keyla Teixeira Santos,[c] Jesús Barrio,[a,b] Viktoriia A. Saveleva,[f] Pieter Glatzel,[f] Vinod K. Paidi,[f] Xiaoyan Li,[g] Andreas Hutzler,[d] Maria-Magdalena Titirici,[b] Antoine Bonnefont,[c] Serhiy Cherevko,[d] Ifan E. L. Stephens,[a,*] Frédéric Maillard[c,*]

a *Imperial College London, Department of Materials, Royal School of Mines, London SW7 2AZ, UK*

b *Imperial College London, Department of Chemical Engineering, London SW7 2AZ, UK*

c *Univ. Grenoble Alpes, Univ. Savoie-Mont-Blanc, CNRS, Grenoble-INP, LEPMI, 38000 Grenoble, France*

d *Forschungszentrum Jülich GmbH, Helmholtz-Institute Erlangen-Nürnberg for Renewable Energy (HI ERN), Cauerstraße 1, 91058 Erlangen, Germany*

e *Friedrich-Alexander-Universität Erlangen-Nürnberg, Department of Chemical and Biological Engineering, Cauerstraße 1, 91058 Erlangen, Germany*

f *ESRF, The European Synchrotron, 71 Avenue des Martyrs, CS40220, 38043 Grenoble Cedex 9, France*

g *Laboratoire de Physique des Solides CNRS, Université Paris Sud, 91405 Orsay, France*

‡ Equal contributions.

Abstract

Atomic Fe in N-doped C (Fe-N-C) catalysts provide the most promising non-precious metal O_2 reduction activity at the cathodes of proton exchange membrane fuel cells. However, one of the biggest remaining challenges to address towards their implementation in fuel cells is their limited durability. Fe demetallation has been suggested as the primary initial degradation mechanism. However, the fate of Fe under different operating conditions varies. Here, we monitor *operando* Fe dissolution of a highly porous and >50% FeN_x electrochemical utilization Fe-N-C catalyst in 0.1 M $HClO_4$, under O_2 and Ar at different temperatures, in both flow cell and gas diffusion electrode (GDE) half-cell coupled to inductively coupled plasma mass spectrometry (ICP-MS). By combining these results with *pre-* and *post-mortem* analyses, we demonstrate that in the absence of oxygen, Fe cations diffuse away within the liquid phase. Conversely, at -15 mA cm^{-2}_{geo} and more negative O_2 reduction currents, the Fe cations reprecipitate as Fe-oxides. We support our conclusions with a microkinetic model, revealing that the local pH in the catalyst layer predominantly accounts for the observed trend. Even at a moderate current density of -15 mA cm^{-2}_{geo} and under O_2 at 25 °C, a significant H^+ consumption and therefore pH increase (pH = 8-9) within the bulk Fe-N-C layer facilitate precipitation of Fe cations. This work provides a unified view on the Fe degradation mechanism for a model Fe-N-C in both high-throughput flow cell and practical operating GDE conditions, underscoring the crucial role of local pH in regulating the stability of the active sites.

1

Introduction

Low temperature proton exchange membrane fuel cells (PEMFCs) powered by green hydrogen provide a means to sustainable energy conversion for stationary and transport applications. Their widespread commercialization is partially limited by the cost of the platinum (Pt)-based nanoparticles supported on high surface area carbon (Pt/C) at the cathode, where oxygen reduction reaction (ORR) occurs. Single iron (Fe), cobalt (Co), manganese (Mn) or tin (Sn) atoms (and their combinations) coordinated to nitrogen-doped carbon (M-N-C, where M is the metal) exhibit the most promising non-precious metal activity for ORR.[1–5] Of these, Fe-N-C has exhibited the greatest PEMFC performance.[6] Still, ~60-100 μm_{Fe-N-C} thick Fe-N-C cathodes are commonly used to compete with the PEMFC performance of ~5 $\mu m_{Pt/C}$ thick Pt-based cathodes,[7] due mainly to Fe-N-Cs lower specific and volumetric active site density.[8–10] With further improvements, Fe-N-C offer a potentially less expensive and less environmentally impactful alternative to Pt/C,[11,12] although highly active Fe-N-C typically suffer from lower durability.[5,13] Researchers have improved the stability of Fe-N-C by improved synthesis pathways, producing atomically dispersed active sites, rather than encapsulated nanoparticles, which induce instability.[14] Most recently adding atomically thin protective coatings or reductive pyrolysis conditions has led to Fe-N-C durability beyond 300 h in PEMFC under H_2/Air.[6,15]

However, Fe-N-C durability is still below commercial realization for transport applications (>5,000 h)[16] owing to several degradation routes,[17] which can be separated into two categories. Firstly, support modification, such as oxidation of the N-C matrix,[2,18,19] and N-protonation (especially for materials synthesized through pyrolysis under ammonia).[20] Second is direct active metal atom modification by agglomeration/ aggregation, and demetallation/dissolution.[18,21,22] The demetallation of the active site can also take place indirectly through chemical or electrochemical corrosion of the N-C matrix.[23] Steps can be taken to deconvolute these degradation pathways[24] and also minimize them,[25,26] or even temporarily reverse them by reactivation.[27] However, studies point towards the demetallation of FeN_x active sites being the primary irreversible performance degradation mechanism in PEMFCs [6,28,29] and the first step in the aggregation scenario.[21]

Inductively coupled plasma mass spectrometry (ICP-MS) is a highly sensitive technique which can provide time- and potential-resolved Fe dissolution profiles from Fe-N-C catalysts. Monitoring Fe dissolution from *ex situ* ICP-MS, in tandem with other characterization techniques, in rotating disc electrode (RDE)[30] and PEMFC has revealed significant dissolution of Fe,[31] although probing the mechanism requires *operando* measurements. In the first online flow cell ICP-MS study, Choi *et al.* suggested formation of insoluble ferric (Fe^{3+}) species, which dissolve under PEMFC operating conditions ($E_{cathode} < 0.7\ V_{RHE}$) due to *operando* reduction to soluble ferrous (Fe^{2+}) cations.[26] This is in line with former *ex situ* ICP-MS findings of Zelenay and coworkers[30] who suggested higher solubility of Fe^{2+} species in acid solutions compared to Fe^{3+} species. Previous online flow cell ICP-MS studies also provided critical information on the effects of pyrolysis atmosphere, bulk electrolyte pH, and catalyst modification on the extent of Fe dissolution.[18,26,32]

Nonetheless, flow cell ICP-MS studies are limited to low current densities, and cannot reproduce all the practical conditions occurring in an operating PEMFC device (O_2 partial pressure and current density, lower relative humidity).[33] In this respect, online gas diffusion electrode (GDE) ICP-MS is an adequate tool to simulate the environment of a PEMFC cathode more realistically, and gain PEMFC-relevant durability trends. For instance, Ehelebe *et al*. first demonstrated significantly lower dissolution of Pt/C catalysts in GDE configuration compared to flow cell systems due to varying mass transport conditions of Pt species,[34] as previously proposed.[35] Very recently, Choi and coworkers[25] monitored *in situ* changes in active site density and *operando* Fe dissolution of a Fe-N-C under Ar and O_2 at different

temperatures using GDE ICP-MS cell in acidic conditions. From site density monitoring, the reduced turnover frequency confirmed a reactive oxygen species catalyzed carbon corrosion scenario.[23,36] However, despite using a GDE, Choi and coworkers current densities at 0.6 V chronoamperometric holds (<10 mA cm$^{-2}_{geo}$) were comparable to values achievable in flow cell (~1-2 mA cm$^{-2}_{geo}$), and not practical PEMFCs. They observed from *post-mortem* transmission electron microscopy (TEM) and energy dispersive X-ray spectroscopy (EDXS) elemental mapping that Fe deposited as Fe_xO_y nanoparticles after O_2 reduction in their Fe-N-C derived from microporous zeolitic imidazolate framework-8 (ZIF-8), confirming earlier findings from Kumar *et al*.[36] Evidence of Fe_xO_y nanoparticle formation in PEMFC-relevant conditions has previously been ascribed to highly active but unstable high-spin FeN_4C_{12} moieties, *via* Mössbauer spectroscopy.[37]

Temperature is also a critical parameter for durability of Fe-N-C catalysts. Goellner *et al*. first evidenced that the rate of corrosion of a N-C matrix (150 square wave cycling between 0.9-1.4 V_{RHE}, 3 s holds in RDE) increases 14-fold when temperatures increase from 20 to 80 ^{o}C. This resulted in 18-fold larger O_2 reduction activity decay (at 0.8 V_{RHE}), which was assigned to N-C corrosion.[38] Carbon corrosion can be avoided at 25 ^{o}C in RDE by keeping potential < 0.9 V_{RHE},[18] although some carbon corrosion (<7 mA cm$^{-2}_{geo}$) is reported in PEMFC at 80 ^{o}C.[22] Kumar *et al.* reported Fe cluster formation under load cycling (Ar-saturated 0.1 M H_2SO_4, 0.6-1.0 V_{RHE}) at 80 ^{o}C, but did not observe Fe clusters at 60 ^{o}C, providing strong evidence of the effect of temperature on the fate of Fe species.[21] Finally, we note that Osmieri *et al*. reported greater performance loss under air-fed *vs*. N_2-fed PEMFC cathode (3 s holds at 0.95 and 0.6 $V_{vs\ anode}$, 80 ^{o}C), although with no nanoparticle formation.[39] There are thus conflicting results in literature, which is could be due to operation conditions, (temperature, gas atmosphere, Nafion content, current densities, potential etc.), storage conditions,[40] electrode preparation[41] and synthesized Fe-N-C properties.[37] Moreover, most of Fe-N-C catalysts studied by *operando* ICP-MS have consisted of low active site utilization Fe-N-C derived from ZIF-8. Our laboratory,[42] and others,[43,44] have highlighted that such catalysts display a predominantly or purely microporous structure. This limits the mass transport and electrochemical active site utilization (number of electrochemically accessible FeN_x sites to the total number of FeN_x sites) to typically <10%.[42–44] This prompted us to revisit Fe dissolution and the fate of Fe in FeN_x active sites from our recently developed high FeN_x utilisation (>50%) Fe-N-C with high micro- and meso-porosity.[42] This pore structure can facilitate mass transport of reactants for improved activity, while also enabling transport of dissolved Fe ions for *operando* ICP-MS detection.

The impact on Fe-N-C activity from changes in the (micro-) environment from RDE to GDE/PEMFC has been discussed.[45–47] Local pH is one value which could vary between electrocatalysts and testing conditions, and is recognized to influence Fe-N-C activity.[48–50] Meanwhile, the influence of pH on degradation is beginning to receive greater attention in modelling reaction mechanisms and dissolution trends.[51] Local pH (at the interface between the working electrode and the bulk of the electrolyte) and its effects has been investigated and discussed quite extensively in electrochemical CO_2 reduction;[52,53] however, so far it has garnered limited experimental and theoretical evidence for ORR.[54–56] Meanwhile, kinetic modelling work by Zenyuk and Litster found during ORR increased pH along Pt mesopore channels, when devoid of Nafion and instead filled with water.[57] It is worth considering that FeN_x active sites are proposed to be located within micropores,[22,43,58] which are expected to be filled with water.[22] Even so, Banham and coworkers' experiments suggest that micropore flooding does not contribute significantly to PEMFC performance decay.[59] Instead, kinetic models of Fe-N-C activity decay under different potentiostatic conditions in PEMFCs have been previously proposed,[22,60,61] which has led to some debate.[62,63] Still, to date these kinetic models of Fe-N-C have not factored in pH change and conditions in GDEs have not been considered.

In this work, we monitored Fe dissolution of a high electrochemical utilization Fe-N-C catalyst using *operando* flow cell and GDE ICP-MS. We found that the fate of Fe-N-C catalysts is determined by combined Fe demetallation, reactive oxygen species action (magnifying Fe demetallation) and local pH changes caused by ORR. We used a suite of complimentary *pre-* and *post-mortem* characterization techniques (SEM, TEM, STEM, EDXS, EELS, Raman spectroscopy, XRD, XPS, XANES) to illustrate changes in structure and chemistry; based on our experimental insights, we built a microkinetic modelling to interpret our observations.

Experimental

Fe-N-C Preparation. TAP 900@Fe and TAP 900@^{57}Fe were prepared according to our previous work,[42] with their synthesis also detailed in the **Supplementary Information**.

Online Flow Cell ICP-MS

The setup consisted of a homemade PEEK cell (**Figure S1**) with a three-electrode configuration using a glassy carbon rod as counter electrode (Sigradur grade G, HTW GmbH) and a leak-free Ag/AgCl/3.4 M Cl$^-$ (ET072, eDAQ) as reference electrode. The Ag/AgCl/3.4 M Cl$^-$ was calibrated versus reversible hydrogen electrode (RHE) via both a Hydroflex (Gaskatel) and a homemade Pt wire RHE. ^{57}Fe in TAP 900@^{57}Fe was used for online flow cell ICP-MS measurement to avoid interference from ArO$^+$. The flow cell protocol and ICP-MS operation is detailed in the **Supplementary Information** and **Figure S2.**

GDE

Electrode Manufacture

The GDEs were prepared by doctor-blade coating an Fe-N-C ink onto a gas diffusion layer (GDL) including a microporous layer (Freudenberg, H23C8, 215.5±6.5 μm). During the doctor-blade coating the temperature of the plate of automated film applicator (Zehntner, ZAA 2300) was at room temperature (23.5±0.5 °C). The composition of the ink was 12 wt.% solutes in a water/alcohol mixture, consisting of 68 wt.% isopropanol (Supelco, EMSURE, ACS ISO), 17.6 wt.% 1-Propanol, 13.6 wt.% water and <0.8 wt.% Ethanol, where the latter three components are from the commercial Nafion solution (Fuel Cell Store, D2021, 21±1 wt.% Nafion, 34±2 wt.% water, 44±2 wt.% 1-Propanol, and < 2 wt.% Ethanol). The solute fraction comprised 41.3 wt.% of TAP 900@Fe material and 58.7 wt.% of Nafion. Due to the high mesopore volume of TAP 900@Fe,[42] a relatively high ionomer to Fe-N-C weight ratio of 1.42:1 was used to ensure utilization of the catalyst layer. After 30 min of stirring and 1 h of sonication (100 W VWR Ultrasonic Cleaner USC 500 THD) at T < 30 °C, the ink was constantly stirring until deposition. After the ink deposition onto the GDL, the samples were dried at room temperature (21±2 °C) under atmospheric pressure until testing. The catalyst layer loading was 0.86±0.15 mg$_{FeNC}$ cm$^{-2}_{geo}$, as determined by weighing the GDE before and after Fe-N-C coating. The catalyst layer thickness was 58±4 μm, as measured by a micrometer (Helios Preisser, 0912501).

Online GDE ICP-MS

Prior to electrochemical testing, GDEs were immersed in ultrapure water for 1 hour. The electrolyte, reference and counter electrodes were 0.1 M HClO$_4$ (Suprapur, Sigma Aldrich), Ag/AgCl (inner and outer compartments filled with 3M KCl and 0.1 M HClO$_4$, respectively, Metrohm) and Ti/Ir mixed oxide grid (METAKEM), respectively. Ag/AgCl/3M KCl was calibrated every day at the temperature of interest ($E_{Ag/AgCl/Cl^-}$ = 0.316 ± 0.011 V$_{RHE}$ at 20 °C and $E_{Ag/AgCl}$= 0.297 ± 0.013 V$_{RHE}$ at 75 °C). A gas humidification system built with two gas washing bottles (Duran) and a heating plate (IKA^{TM} RCT Basic Hot Plate

4

Stirrer) was used to heat the purged gases to 75 °C. The GDE half-cell was heated to 74 ± 1 °C using an electrolyte recirculation system via a heating bath (AQUAline, LAUDA). In GDE, following the previously reported protocol,[64] 100% post *iR* correction was applied for O_2 measurements, while for Ar measurements, 50% was applied *in situ* and 50% post Ar experiment. Details of GDE ICP-MS operation and protocol are detailed in the **Supplementary Information**, **Table S1** and **Figure S3**. The online Fe dissolution was measured with our previously reported GDE ICP-MS setup,[34,65] shown in **Figure S4**.

Microkinetic Modelling

A one-dimensional model was developed to describe pH distribution in the catalyst layer. This model encompasses a system of partial differential equations (**Supplementary Information**) that account for the transport of Fe and protons in the electrolyte and the 60 μm thick catalyst layer, as well as the proton consumption by the ORR and the dissolution/precipitation of Fe cations in the catalyst layer. The modelling is based on the following assumptions:

(i) The ORR kinetics in the GDE is limited by proton mass transport, with the O_2 concentration being uniform in the catalyst layer.
(ii) The dissolution and precipitation of Fe cations occurs in the water present in the pores *i.e.,* the precipitation of Fe cations is not influenced by the Nafion ionomer in the catalyst layer:
$Fe^{3+} + 3 H_2O \rightarrow Fe(OH)_3 + 3 H^+$
(iii) Due to the pronounced difference in complexation constants, only Fe^{3+} cations are expected to precipitate.[66] If Fe^{2+} cations are dissolved in water, they will anyway thermodynamically be oxidized into Fe^{3+} cations by O_2.[67]
(iv) Based on the GDE ICP-MS data at 20 °C that will be discussed later, the rate of production of dissolved Fe ions is assumed to be approximately two times faster in O_2 than in Ar GDE experiments.
(v) A homogeneous potential distribution is assumed in the catalyst layer.

Results

Comparing TAP 900@Fe and TAP 900@^{57}Fe RDE ORR Activity

Thorough *ex situ* characterization of TAP-derived materials was carried out in our previous work.[42] Although some comparisons between TAP 900@^{57}Fe and TAP 900@Fe were missing. Considering O_2 reduction, reduced activity has previously been reported for ^{57}Fe enriched Fe-N-C samples compared to Fe-N-C prepared in the same manner but with natural abundance Fe precursor.[68] The RDE O_2 reduction mass activity for TAP 900@^{57}Fe and TAP 900@Fe can be found in **Figure S5**a-b. The kinetic region and mass activity at 0.8 $V_{RHE, iR-free}$ in O_2-saturated RDE is lower in TAP 900@^{57}Fe compared to previously reported TAP 900@Fe,[42] with 3.77±0.54 and 5.01±0.79 A g_{FeNC}^{-1}, respectively (**Figure S5**a). The lower activity with ^{57}Fe enrichment follows the previous report.[68]

Online Flow Cell ICP-MS

Moving to *operando* flow cell ICP-MS measurements in 0.1 M $HClO_4$, TAP 900@^{57}Fe was used to avoid polyatomic interference from ArO^+ and maximize spectrometric signal. The setup and experimental protocol are depicted in **Figure S1** and **Figure S2**, respectively. First, ICP-MS calibration, electrochemical impedance spectroscopy and open circuit potential (OCP) measurements were conducted to ensure correct installation and operation. Next, 50 fast (50 mV s^{-1}) cyclic voltammograms (CV) between 0.925-0.200 V_{RHE} were measured in Ar-saturated electrolyte to allow the catalyst to reach a stable electrochemical and dissolution measurement (**Figure 1**a, 0.2 mg$_{FeNC}$ cm$^{-2}_{geo}$). Mg was also monitored during the initial 50 cycles due to its use as a templating agent during synthesis, with 0.06 wt.%

detected from *ex situ* ICP-MS in our previous work.[42] Mg dissolution did not vary with potential (**Figure 1**a) and so is not considered further. Meanwhile, the rate of Fe dissolution followed an exponential decay.
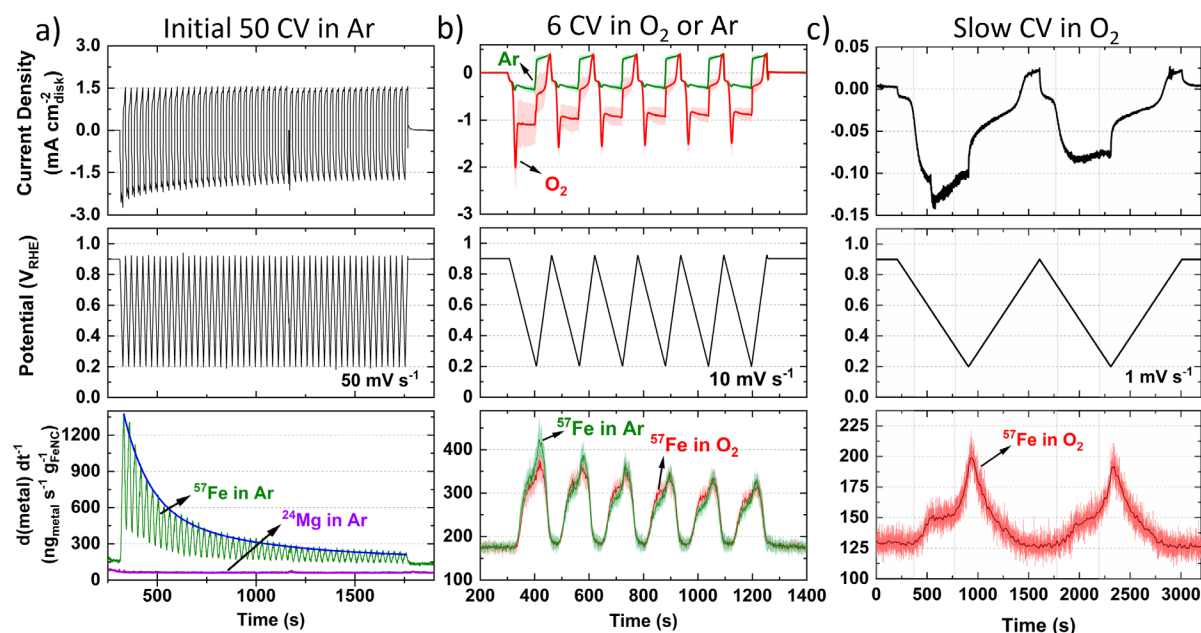

Figure 1. Online flow cell ICP-MS metal dissolution during a.) Initial 50 CVs at 50 mV s^{-1} under Ar-saturated 0.1 M HClO$_4$ with 0.2 mg$_{FeNC}$ cm^{-2}. Blue line represents fitted exponential decay. b.) Six CV at 10 mV s^{-1} under Ar- (green) and O$_2$- (red) saturated conditions. Error represents standard deviation from four separate measurements. c.) Two slow CV scans at 1 mV s^{-1} under O$_2$-saturated 0.1 M HClO$_4$ with 0.2 mg$_{FeNC}$ cm^{-2}. Dark red line represents fast Fourier transform smoothed data.

Considering the effect of increased Fe-N-C loading, the amount of ^{57}Fe dissolution follows a linear trend over the initial 50 CVs (**Figure S6**a). The percentage of total ^{57}Fe detected increases from 7.5±2.9% to 15.2±3.3% as catalyst loading increases from 0.05 to 0.40 mg$_{Fe-N-C}$ cm$^{-2}_{geo}$, with 11.3±5.6% at 0.20 mg$_{Fe-N-C}$ cm$^{-2}_{geo}$ (**Figure S6**b). This finding appears counterintuitive as one would expect either an equivalent percentage of Fe detected relative to the loading, or even a reduced percentage of detected Fe, due to reduced active site utilization with increasing thickness of the catalyst layer. It is also worth noting that there is a constant 130 ng$_{Fe}$ g$_{FeNC}^{-1}$ s^{-1} ^{57}Fe concentration observed when held at 0.9 V$_{RHE}$ (**Figure 1a-c**), which was also the OCP of the TAP 900@^{57}Fe catalyst.

After the initial 50 CVs at 50 mV s^{-1}, six CVs were conducted at 10 mV s^{-1} under Ar and then O$_2$-saturation. With increasing TAP 900@^{57}Fe loading under O$_2$-saturation, the limiting current density (below 0.65 V$_{RHE}$) only incrementally increases. This slight increase can be explained by the increasing thickness of the catalyst layer with loading, which penetrates deeper into the flowing O$_2$-saturated electrolyte. Meanwhile, between 0.65-0.80 V$_{RHE}$ there is an increasing O$_2$ reduction peak in the cathodic direction (**Figure S7**a). This is caused by a build-up of O$_2$ concentration locally in the catalyst layer while scanning the potential region of 0.800-0.925 V$_{RHE}$, where very little ORR is observed.

Under Ar-saturated conditions the current density increases proportional to the catalyst loading; we note there is an increasing peak on the cathodic scan (**Figure S7**b). We attribute this cathodic peak to the reduction of trace O$_2$, arising from air ingress at the junction of the Kalrez O-ring and cell (or cavitation from the peristaltic pump). Still, the amount of O$_2$ appears negligible. Normalizing the ^{57}Fe detected to charge passed and catalyst loading shows the amount of ^{57}Fe detected is constant under O$_2$ but increases with reduced catalyst loading under Ar (**Figure S7**c-d). Meanwhile, the amount of ^{57}Fe

6

detected is equivalent under either gas saturation, with 1.3-2.0% of total ^{57}Fe detected, and linear dependence with Fe-N-C loading (**Figure S7**e-f). Focusing on the dissolution at 0.2 mg_{FeNC} cm^{-2}_{geo}, similar profiles are observed under Ar and O_2-saturation (**Figure 1**b).

To better distinguish the Fe dissolution features, slow CVs (1 mV s^{-1}) were conducted under O_2-saturation (**Figure 1**c). The slow scans show two onsets of ^{57}Fe dissolution above background levels on the cathodic scan at *ca.* 0.72 and 0.33 V_{RHE} (**Figure 1**c).

To evaluate differences in Fe detection and profiles over a longer period, 1 h AST or chronoamperometry (CA) were recorded in 0.1 M HClO$_4$ (**Figure 2**a-b) or 0.05 M H$_2$SO$_4$ (**Figure 2**c). Greater ^{57}Fe loading-normalized concentration is observed over the course of the AST under O_2 than Ar. ^{57}Fe concentration follows a slow decline under O_2 and rapid plateau above baseline under Ar (**Figure 2**a). 2.7±0.1% of total ^{57}Fe is detected during O_2 AST (**Figure 2**d), with a charge normalized Fe dissolution of 503±3 ng_{Fe} mg_{FeNC}^{-1} C^{-1} (**Figure 2**e). Meanwhile, half ^{57}Fe concentration is observed under Ar AST (**Figure 2**d, **Figure S8**); however, normalizing to the total charge passed shows approximately double, with 1022 ng_{Fe} mg_{FeNC}^{-1} C^{-1} (**Figure 2**e). *Pre-* and *post-mortem* bright-field TEM of these samples shows no formation of detectable nanoparticles under Ar or O_2 (**Figure S9**), indicating all Fe demetallation leads to dissolution at 25 °C, in agreement with former findings of Kumar *et al.*[36]

CA under O_2 at 0.2 V_{RHE} shows a large initial spike in ^{57}Fe concentration, which then decays over time, while CA at 0.6 V_{RHE} shows a smaller spike and lower overall dissolution (**Figure 2**b). The initial spike in ^{57}Fe concentration may be related to double layer charging and rapid change in potential. After 30 mins, the current density and Fe dissolution are equivalent at 0.2 and 0.6 V_{RHE} CA. CA at 0.2 V_{RHE} ends with 4.6±0.4% of total ^{57}Fe and 686±166 ng_{Fe} mg_{FeNC}^{-1} C^{-1}. This is approximately double the values at 0.6 V_{RHE}, with 2.2±0.1% ^{57}Fe and 358±61 ng_{Fe} mg_{FeNC}^{-1} C^{-1} (**Figure 2**e). This correlates with the observations from **Figure 1**c, where greatest Fe dissolution occurs around 0.20 V_{RHE}.

At the same pH in 0.05 M H$_2$SO$_4$ instead of 0.1 M HClO$_4$, O_2 AST shows a similar dissolution profile, with lower Fe detection but higher O_2 current densities (**Figure 2**c). This difference in current is unexpected as O_2 solubility is comparable at these acid concentrations. Meanwhile the total ^{57}Fe loss is 2.3±0.1% in 0.05 M H$_2$SO$_4$ and slightly higher in 0.1 M HClO$_4$ with 2.7±0.1% (**Figure 2**d). However, the charge normalized Fe dissolution is less than half in 0.05 M H$_2$SO$_4$, at 231±63 ng_{Fe} mg_{FeNC}^{-1} C^{-1} (**Figure 2**e).
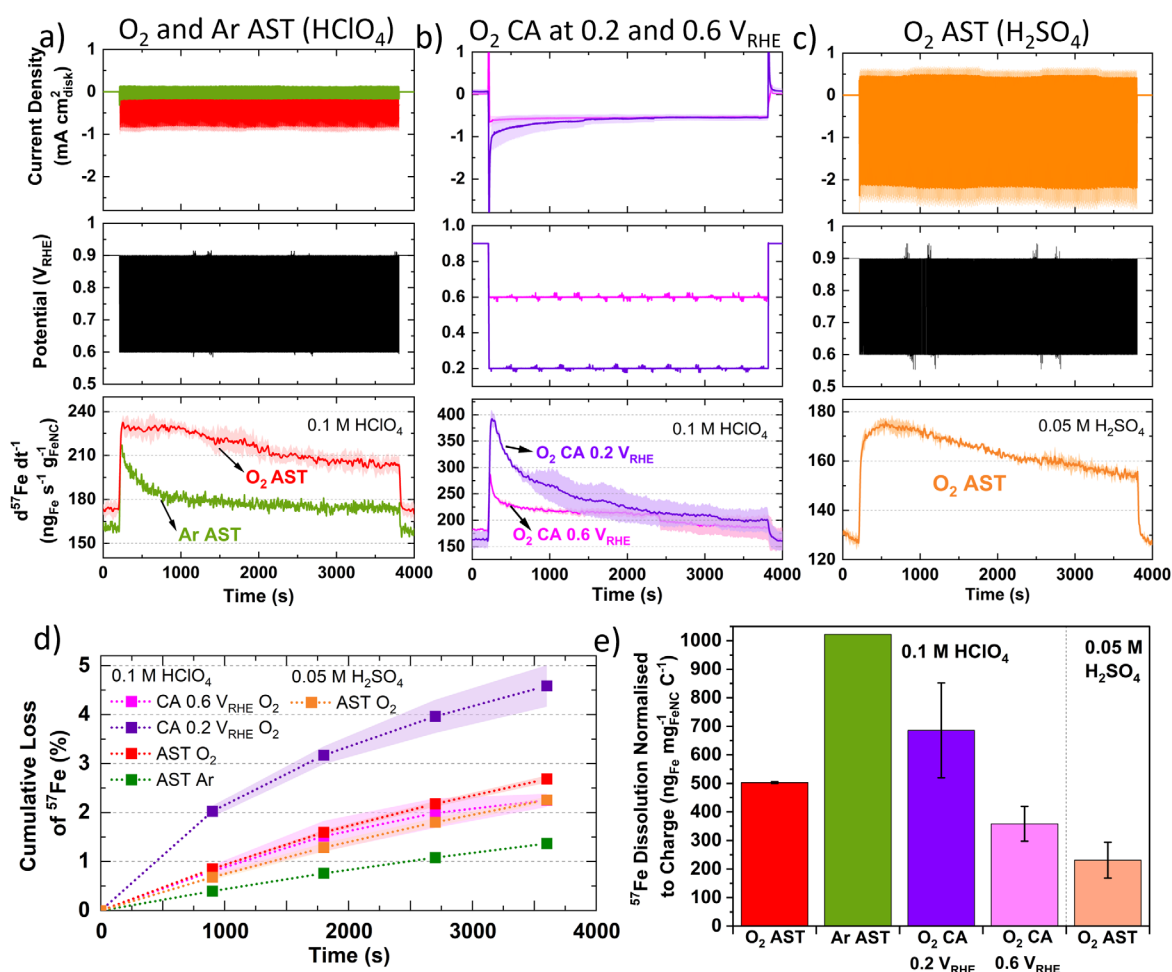
Figure 2. Online flow cell ICP-MS of TAP 900@^{57}Fe a.) AST (3 s hold at 0.9 and 0.6 V_{RHE}) under Ar- and O$_2$-saturated 0.1 M HClO$_4$. b.) 0.2 and 0.6 V_{RHE} CA in O$_2$-saturated 0.1 M HClO$_4$ c.) AST under O$_2$-saturated 0.05 M H$_2$SO$_4$. Lighter shaded region represent error from two measurements. d.) Cumulative Fe loss. e.) Charge normalized Fe dissolution over varying stability test conditions. All tests over 1 h with 0.2 mg$_{FeNC}$ cm^{-2}$_{geo}$. Error in figures represent two repeat measurements.

GDE O$_2$ Reduction and Degradation

While flow cell measurements proved insightful, the degradation rate in real PEMFCs may be different due to higher ORR rates and therefore ORR charge passed. To reach higher current densities and conditions comparable to PEMFCs, TAP 900@Fe was tested in a GDE half-cell coupled to online ICP-MS in 0.1 M HClO$_4$ at 21±1 °C and 74±1 °C, denoted as 20 and 75 °C herein.

Based on flow cell results, 50 CVs under Ar-saturation (50 mV s^{-1}, 0.9-0.2 V_{RHE}, **Figure S10**) were initially carried out to remove loosely bound Fe. O$_2$ reduction was measured in GDE half-cell before and after AST tests (**Figure 3**a-b,). Catalyst loadings varied between 0.7 to 1.0 mg$_{FeNC}$ cm^{-2}$_{geo}$, consequently corresponding mass activity plots are shown in **Figure S11**a-b. Compared to initial 20 °C O$_2$ reduction, after 20 °C Ar AST there is an apparent improvement in O$_2$ reduction performance at current densities up to -50 mA cm^{-2}$_{geo}$ (**Figure 3**a). This is assigned to improved wetting of TAP 900@Fe during the 20 °C Ar AST. Meanwhile, 20 °C O$_2$ AST led to noticeable performance degradation after only 200 cycles, with potential shift at -50 mA cm^{-2}$_{geo}$ of -50±30 mV (from 0.61±0.03 to 0.56±0.00 $V_{RHE, iR-free}$) compared to pristine 20 °C TAP 900@Fe (**Figure 3**a). At -50 mA cm^{-2}$_{geo}$, 75 °C GDE pristine TAP 900@Fe shows an

8

improved O_2 reduction potential of 0.68±0.01 $V_{RHE, iR-free}$. Although, 75 °C O_2 200 AST cycles results in severe degradation to 0.58±0.03 $V_{RHE, iR-free}$ (**Figure 3**b).

Pre- and Post GDE Protocol Characterisation

XPS peak fitting of fresh GDE C1s and O1s spectra is provided in **Figure S12**a-b with comparison of O1s between pre and post GDE protocol in **Figure 3**c. Comparison of O1s XPS spectra for fresh GDE and after 20 °C Ar and O_2 protocols shows comparable total O1s of 8.9-8.1 at.% (**Figure S12**c, **Table S3**), with slight reductions in C=O and C-O peaks for AST samples (**Figure 3**c). Meanwhile, after 75 °C O_2 protocol, a clear overall O1s increase is found, equivalent to 12.2 at.% O1s (**Figure S12**c). There is less discernible change in the C1s spectra, aside from reduction in C-N and C-C and increase in CF2 in all AST samples compared to the pristine TAP 900@Fe GDE (**Figure S13**). Raman spectra (**Figure S14**) for pristine and post Ar and O_2 20 °C GDE protocols show no discernable difference (I_d/I_g = 1.02-1.03, based on peak height), while there is a slight increase after 75 °C O_2 protocol (I_d/I_g = 1.05), indicating a minor increase in defects in the carbon structure.

Within the pristine TAP 900@Fe GDE no visible nanoparticles are detected using HAADF-STEM and STEM-EDXS spectrum imaging (**Figure 3**d, **Figure S15**a). After 20 °C Ar protocol, one large Fe_xO_y nanoparticle is detected in the spectrum image, while, at higher magnification, small clusters are observed (**Figure 3**e, **Figure S15**b). Numerous Fe nanoparticles are observed following 20 °C O_2 protocol in GDE, which are assigned to Fe_xO_y based on overlaying the Fe and O EDXS mapping (**Figure 3**f, **Figure S15**c). HAADF-STEM combined with EDXS and EELS reveals clusters containing Ca and Fe in fresh and post Ar and O_2 AST GDE (**Figure S16**). The presence of Ca remains unexplained, as we consistently used MQ water for all our electrochemical experiments and rinsing steps. No trace of Ca was also detected in the native catalyst. We therefore attribute it to contamination by tap water. The peak at 695 eV is from Fe-K. STEM-EELS analysis in regions without Fe particles cannot resolve any Fe peak (**Figure S16**), likely owing to the concentration of FeN_x sites being below the limit of detection.

Post 75 °C O_2 protocol no large Fe_xO_y particles are seen from EDXS and limited Fe clusters from HAADF-STEM (**Figure 3**g, **Figure S15**d). No significant change from the pristine TAP 900@Fe structure is observed after 20 °C O_2 and Ar protocols, (**Figure S17**a-c); however, after 75 °C O_2 protocol a denser particle structure is observed (**Figure S17**d).

XRD on *post-mortem* GDE AST samples was conducted to try and deduce the type of Fe_xO_y, however either the lack of crystallinity, small particle size and/or low concentration meant no sharp peaks relating to Fe particles could be identified (**Figure S18**). The peak at 18.0° is assigned to polytetrafluoroethylene, which arises from the Nafion backbone. It is worth mentioning that pristine TAP 900@Fe does not show a graphite peak at ~25.6° (002), suggesting its amorphous or graphene-like structure, with an average of single atomic layers found from previous Raman analysis.[69]

Normalized absorption and first derivative XANES of fresh TAP 900@Fe powder and GDE ink, plus post Ar and O_2 25°C protocols, are compared to references of Fe foil, FeO and Fe_2O_3 in **Figure S19**a-d. A positive shift of center of mass of the pre-edge in TAP 900@Fe ink and after Ar and O_2 protocols signifies an increase of oxidation state, while their decrease in intensity is related to a change in local coordination of Fe. TAP 900@Fe GDE ink displays a near identical spectra to post 25°C O_2. This suggests changes in Fe coordination and oxidation state between TAP 900@Fe powder and its ink, similar to a recent report by Saveleva *et al.* for other Fe-N-Cs.[41] Post Ar protocol shows a lower rising edge position indicating a lower average Fe oxidation state, or change in bond length and/or coordination change.
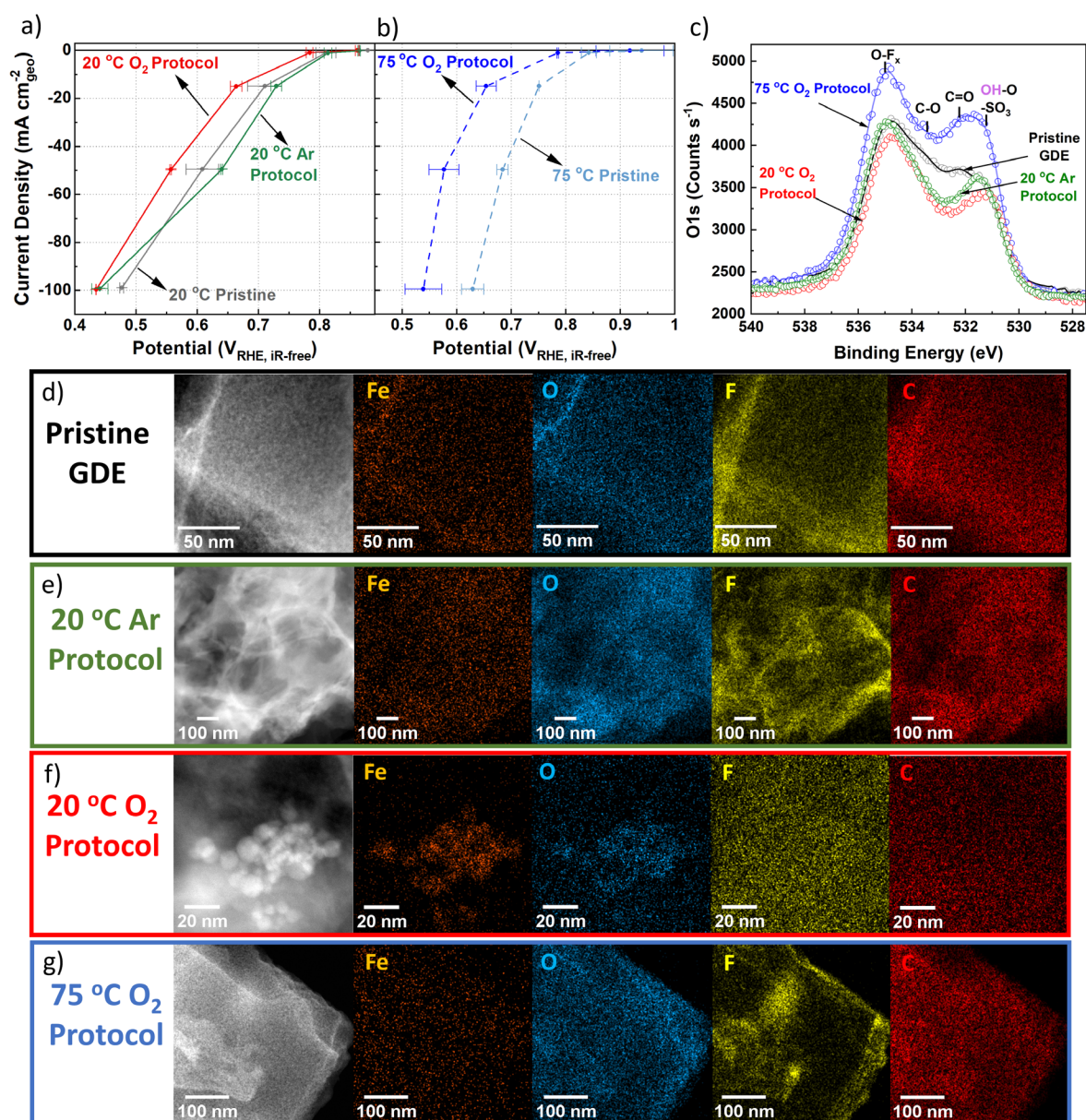
9

Figure 3. GDE polarization curves in 0.1 M $HClO_4$ with 0.7-1.0 mg_{FeNC} cm^{-2}_{geo} for a.) 25 ^oC O_2 reduction in GDE for pristine TAP 900@Fe, and after O_2 and Ar AST. b.) 75 ^oC O_2 reduction in GDE for pristine TAP 900@Fe and after 75 ^oC O_2 AST. Error represents two repeat measurements. 100% post iR correction was applied for O_2 measurements. Comparison of pristine and post protocol GDEs c.) O1s XPS d-g.) HAADF-STEM and STEM-EDXS.

Online GDE ICP-MS

To elucidate the Fe dissolution mechanisms in a practical device, online GDE ICP-MS was measured before, during and after the AST (**Figure 4**) for each of the conditions. It is observed that the baseline Fe concentration is high even after the preliminary 50 CVs in Ar (50 mV s^{-1}).

For initial 20^oC Ar (**Figure 4**a), Fe concentration above baseline occurs at 0.83 $V_{RHE, iR-free}$ and reaches a maximum concentration between 0.64-0.48 $V_{RHE, iR-free}$. Returning to 0.83 $V_{RHE, iR-free}$, Fe concentration returns to baseline levels. Initial 20 ^oC O_2 current step holds (**Figure 4**a) show a lower baseline Fe concentration than 20^oC Ar. A fall in Fe concentration below baseline levels is observed when increasing current density from -1 to -15 mA cm^{-2}_{geo}, corresponding to 0.85±0.02 to 0.80±0.01 $V_{RHE, iR-free}$, respectively. When returning anodically to hold at -1 mA cm^{-2}_{geo}, Fe concentration increases and

10

only begins falling back to baseline once returning to hold at -0.05 mA cm$^{-2}_{geo}$. Initial 75 ^{o}C O$_2$ current hold measurements show a higher baseline Fe concentration, with increased Fe concentration during holds at -1 to -15 mA cm$^{-2}_{geo}$. Fe concentration then returns to approximate baseline values during holds at -50 and -100 mA cm$^{-2}_{geo}$, corresponding to 0.66±0.04 and 0.62±0.04 V$_{RHE, iR-free}$, respectively. Returning anodically to holds at -15 and -0.6 mA cm$^{-2}_{geo}$ results in increased Fe concentration.

Moving to online AST monitoring (**Figure 4**b), 20 ^{o}C Ar shows increased Fe concentration at the beginning of the AST. Fe concentration then gradually decreases over time and falls back to baseline levels after the AST. To note, AST O$_2$ have the same number of cycles (200) in protocol as Ar (3 s holds at each potential), but O$_2$ ASTs took a longer duration because of the additional time to switch the applied current ranges between 3 s holds, which is not required in Ar AST protocol. During the AST, 20 ^{o}C O$_2$ shows a similar Fe concentration profile to current hold prior to AST (**Figure 4**a), with an initial Fe concentration spike, followed by reduced Fe concentration below baseline levels. Fe concentration then returns to baseline levels post AST, without displaying a dissolution spike. 75 ^{o}C O$_2$ also shows an initial spike in Fe concentration at the beginning of the AST, but then maintains baseline Fe concentration values during and post AST with no discernable change.

Post AST (**Figure 4**c), 20 ^{o}C Ar show Fe concentration significantly decreases across the whole potential range compared to prior to the AST (**Figure 4**a). This suggests unstable Fe species have been depleted over the AST. Current step holds after 20 ^{o}C O$_2$ AST show a similar Fe concentration profile to measurements prior to AST, although a higher Fe concentration spike is observed post AST when stepping from -1 to -15 mA cm$^{-2}_{geo}$ (**Figure 4**c). Post AST 75°C O$_2$ shows a symmetric Fe concentration profile when increasing and decreasing current. 75°C O$_2$ GDE ICP-MS results correlate with HAADF-STEM and STEM-EDXS observations (**Figure S15**d), where more Fe has dissolved rather than redeposited as particles, as is the case from 20 ^{o}C O$_2$.
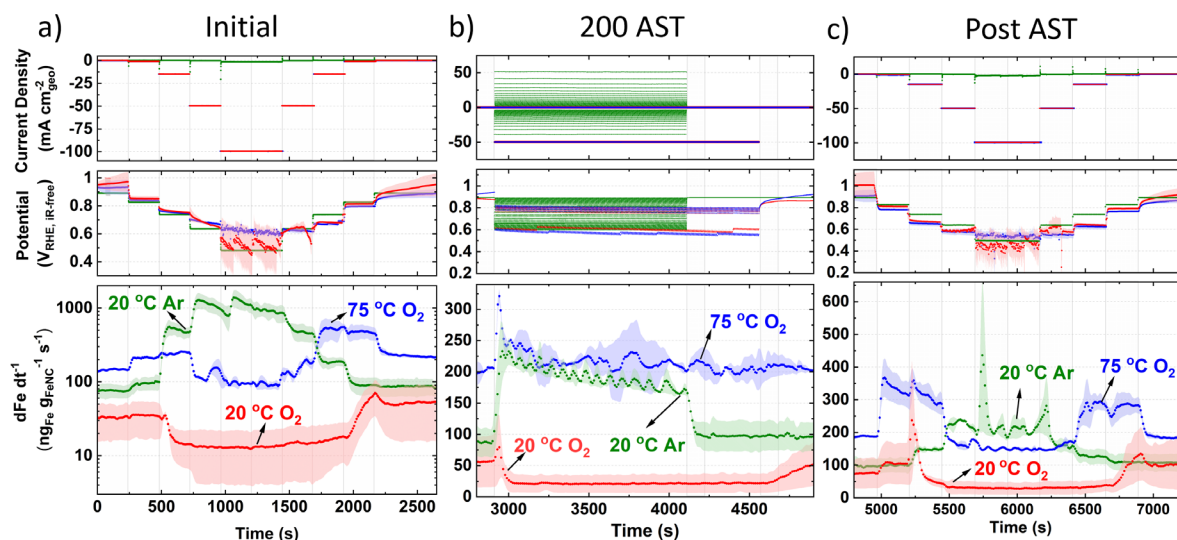

Figure 4. Fe concentration under Ar and O$_2$ at 20 ^{o}C and O$_2$ at 75 ^{o}C in online GDE ICP-MS with 0.1 M HClO$_4$ and 0.7-1.0 mg$_{FeNC}$ cm$^{-2}_{geo}$ a.) prior to AST (note y-axis is log-scale only in a). b.) 200 AST cycles. Under O$_2$, the current was held for 3 s intervals 200 times at -0.05 and -50 mA cm$^{-2}_{geo}$, corresponding to ca. 0.85 and 0.6 V$_{RHE, iR-free}$, respectively. Under Ar, the potential was held for 3 s intervals 200 times between 0.9 and 0.6 V$_{RHE, iR-free}$. c.) Post AST. Error represents two repeat measurements.

Discussion

We now discuss all the results with the aim of establishing similarities or differences between the trends observed on our catalytic material and others.

Flow Cell ICP-MS

Our experiments in flow cell ICP-MS first confirm that the dissolution of Fe atoms is indeed the predominant degradation mechanism in this type of catalyst. In CV, two well-defined Fe dissolution peaks can be observed, with onset of 0.73 and 0.33 V_{RHE} on the cathodic scan (**Figure 1**c). The two ^{57}Fe concentration peaks could represent two different Fe species dissolving at different potentials, or different dissolution process with different formal potentials. Only one Fe concentration peak was resolved by Santori *et al.*, with an onset of Fe concentration at *ca*. 0.75 V_{RHE} for their Ar-pyrolysed Fe-N-C in O_2-saturated 0.1 M H_2SO_4 at 2 mV s^{-1} (data reproduced in **Figure S20**).[32] Meanwhile Choi *et al.* observed the onset of increased Fe concentration at 0.77 V_{RHE}, with two distinguishable Fe dissolution peaks,[18] as observed here. The potential at which peak Fe concentration occurs is not discussed as this depends on mass transport, which changes with the electrochemical cell design and operating conditions.

We note that the onset of increased ^{57}Fe concentration at *ca.* 0.73 V_{RHE} on the cathodic scan (**Figure 1**c) coincides with the onset of the quinone-hydroquinone redox on the cathodic scan post 8,000 O_2 AST at 80°C (**Figure 2c**), and the second peak onset of increased ^{57}Fe concentration at 0.33 V_{RHE} on the cathodic scan coincides with the onset of the second reversible redox on the cathodic scan. Our observations suggest that the stability of the Fe centre may be intrinsically linked to the chemistry of the surrounding ligands; this notion is analogous to relationships observed by others between the catalytic activity and the chemistry of the surrounding ligands.[23,70]

We also note an initial exponential decay in Fe concentration (**Figure 1**a), which was also observed by Choi *et al.* for their Fe-N-C catalyst.[18,26] In our case maximum Fe concentration is observed instantaneously upon potential cycling in Ar, whereas in the report of Choi *et al.* maximum Fe concentration is reached after 2-3 CVs.[18,26] This could be due to the vastly different catalyst structures between our highly micro- and mesoporous TAP 900@^{57}Fe with high active site utilization,[42] and the bulky particle and predominantly microporous ZIF-8 derived Fe-N-C of Choi *et al*.[18,26] Alternatively, it could arise from mass transport effects from slow residence time in Choi *et al.*'s flow cell design. The structure of unmodified microporous ZIF-8 derived materials will have impeded mass transport, low active site utilization and therefore delayed detection of Fe dissolution. Differences in experimental setup and residence time calibration in this work and that of Choi *et al.* could also contribute to the observed time difference in Fe concentration detection.

Choi *et al*.[26] detected ~3% of total Fe over their initial 20 CVs in Ar-saturation (100 mV s^{-1}, 0.8 mg$_{Fe-N-C}$ cm^{-2}) for their purely microporous ZIF-derived Fe-N-C. While after 50 CVs (50 mV s^{-1}, 0.4 mg$_{Fe-N-C}$ cm^{-2}), TAP 900@^{57}Fe shows 15.2 ± 3.3% Fe detected. This again points to the different porosity and structure in TAP- and ZIF-derived materials, leading to different accessibility of Fe sites. Although, it should be noted, according to our previous *ex situ* TAP900@^{57}Fe Mössbauer assignments, *ca*. 11% of the Fe existed as inactive FeCl$_2$·4H$_2$O.[42] This species may represent some or all of the initially dissolved Fe species.

Results from **Figure 1**b (and **Figure S7**e-f) suggest that the Fe concentration is independent of O_2 reduction under cyclic voltammetry (0.9-0.2 V_{RHE} at 10 mV s^{-1}) in flow cell. This is contrary to what is observed in **Figure 2**a, where detected Fe concentration is greater under O_2 than Ar under AST (step from 0.9 to 0.6 V_{RHE} with 3 s potential holds) flow cell conditions. These difference observations of Fe

concentration may be due to either the different potentials scanned (AST: 0.9-0.6 V_{RHE} versus CV: 0.925-0.2 versus), the potential scanning protocol (AST: 3 s square wave voltammetry holds versus CV: 10 mV s^{-1}), or 6 CVs not providing enough cycles to distinguish changes in Fe concentration.

Considering **Figure 2**e and **Figure S8**, Zelenay and coworkers also observed from *ex situ* ICP-MS that $HClO_4$ dissolved more Fe from their polyaniline-derived Fe-N-C than H_2SO_4, which they attributed to differences in solubility of Fe perchlorates and sulfates.[30] We suggest this observation could also be attributed to the stronger SO_4^{2-} binding on the Fe site,[71] whereas ClO_4^- has been proposed to mimic non-specifically adsorbing properties of perfluoro sulfonic acid ionomers.[72] If true, this would imply AST measurements in H_2SO_4 in RDE and GDE would lead to slower FeNC degradation than in $HClO_4$ (at the same pH), when Fe dissolution is the main degradation mechanism.

The different current density under 0.1 M $HClO_4$ and 0.05 M H_2SO_4 (**Figure 2**a and c) may be related to kinetic effects of the proton donor.[73] Additionally, at 0.8 V_{RHE} Fe-N-Cs have recently been reported to possess 1.3-2.9 higher mass activity in H_2SO_4 than $HClO_4$.[71]

GDE ICP-MS

Under initial Ar in GDE ICP-MS (**Figure 4**a), the most significant increase in Fe concentration occurs when the potential drops from 0.83 to 0.74 V_{RHE}. This can be explained by the Fe^{3+}/Fe^{2+} redox transition at 0.76 V_{RHE} (**Figure S10**). It is worth noting that with a Fe-N-C, Fe atoms possess different formal redox and dissolution potentials depending on their coordinating ligands and extended local environment (number and size of graphene sheets,[74] oxygen functional groups[23,27]). This broad Fe^{3+}/Fe^{2+} redox range is also initially observed in **Figure S10**. Moreover, after the increases of Fe concentration during cathodic potential shifts, gradual declines in the Fe concentration are frequently observed. This is related to the fact that the location of the Fe within the Fe-N-C structure (outer catalyst layer surface or deeper within) affects the transfer function and hence residence time.

It has been previously suggested that O-containing groups on the carbon surface reduce the turnover frequency of Fe-N-Cs by weakening O_2-binding on FeN_x sites.[23] The limited change in XPS O1s spectra between pristine and 20 °C O_2 GDE protocol (**Figure 3**c) suggests performance degradation from 20 °C O_2 protocol (**Figure 3**a) is mainly attributed to active site demetallation. Meanwhile, the increase in O1s after 75 °C O_2 protocol (**Figure 3**c) causes reductions in TOF and FeN_x sites' stability[19] and the increased observation degradation. Reduction in TOF occurs due to reactive oxygen species catalyzing mild carbon corrosion.[23,36]

The rapid decay in O_2 reduction performance (*e.g.* -50±30 mV at 50 mA cm^{-2}_{geo} after 200 cycle AST in 20 °C O_2) and high Fe dissolution can be attributed to the high percentage of unstable high spin $Fe^{3+}N_x$ present (assuming the same type of sites are present between TAP 900@^{57}Fe and TAP 900@Fe). Additionally, according to density functional theory (DFT) calculations for Fe-N-C, the number and size of graphene sheets affects the Fe dissolution potential.[74] Previous Raman analysis of TAP 900 determined an atomically thin carbon structure,[69] which therefore leads itself to possess less stable FeN_x sites.

The online GDE ICP-MS concentration profile under 20 °C O_2 (**Figure 4**a and c) suggests Fe dissolution and subsequent detection by ICP-MS at low current density (-0.05 to -1.00 mA cm^{-2}_{geo}). Meanwhile, at higher current density (-15, -50 and -100 mA cm^{-2}_{geo}), a process of Fe dissolution and redeposition locally into Fe_xO_y in the catalyst layer is proposed. This is supported by the increased observation of Fe_xO_y after O_2 GDE protocol from HAADF-STEM and EDXS (**Figure 3**f and **Figure S15**). The reason for Fe_xO_y formation is hypothesized to arise based on the Fe Pourbaix diagram, where an increase in the local pH would form Fe_2O_3. This pH increase in the catalyst layer could occur due to the rapid

13

consumption of H^+ during increased O_2 reduction currents ($4H^+ + O_2 + 4e^- \rightarrow 2H_2O$). It is then expected that some Fe_xO_y redissolves when returning anodically to low O_2 reduction current density (-1 mA cm$^{-2}_{geo}$), due to a return to acidic pH. This redissolution is evidenced by the detected increase in Fe concentration at -1 mA cm$^{-2}_{geo}$ on the anodic step for 20 $^{\circ}$C O_2 in GDE ICP-MS. The observation of Fe_xO_y corroborates previous findings from *post-mortem* O_2 AST protocols.[36,37] Moreover, the increased Fe concentration detected when stepping the potential down in the cathodic direction after post AST (**Figure 4**c) for O_2 GDE at 20 $^{\circ}$C and 75 $^{\circ}$C supports the hypothesis that Fe_xO_y builds up in the catalyst layer at current densities of -50 mA cm$^{-2}_{geo}$ during the AST and is only released at lower current density holds (-1 mA cm$^{-2}_{geo}$ at 20 $^{\circ}$C and 75 $^{\circ}$C).

Mass transport (O_2 solubility and H^+) and the thermodynamics and kinetics of ORR and Fe dissolution (at a constant potential on the RHE scale) will all change with temperature.[75] This makes it challenging to deconvolute their contributions to changes in performance; however, kinetic modelling based on experimental data can help explain phenomena, such as local pH changes.

Kinetic Modelling

We developed a microkinetic model of the system (**Figure 5a** and **Supporting Information**) to replicate the observations from GDE ICP-MS prior to AST at 20 $^{\circ}$C in 0.1 M $HClO_4$ and evidence our hypothesis on the pivotal role of local pH. The model assumed the initial proton concentration and potential in the catalyst layer is homogeneous. We focus on the Fe concentration observed in GDE ICP-MS at 0.75 $V_{RHE, iR-free}$ and 20 $^{\circ}$C, corresponding to a current density of -15 and 0 mA cm$^{-2}_{geo}$ under O_2 and Ar supply, respectively. The void volume (ε) in the catalyst layer was adjusted to semi-quantitatively simulate the time evolution of the Fe concentration signal monitored by GDE ICP-MS in Ar-saturated electrolyte (**Figure 5**b and c). The value of the proton consumption rate constant (k_r) and ε were then varied to replicate the Fe concentration signal measured in O_2-saturated electrolyte (**Figure** 5b-d). Good agreement between experiment and simulation are reached for the range of values considered ($0.2 \leq \varepsilon \leq 0.4$ and $100 \leq k_r \leq 400$ s^{-1}). Additionally, values for the tortuosity factor, τ ($=1/\sqrt{\varepsilon}$) were within previously reported ranges ($1.8 \leq \tau \leq 2.2$).[76,77]

Figure 5e displays the corresponding simulated pH profile in the catalyst layer. The simulations predict a significantly lower concentration of detected Fe cations during O_2 reduction (**Figure 5**d). This phenomenon is attributed to the precipitation of Fe^{3+} cations under the local conditions in the catalyst layer, with the Fe concentration resulting from the balance between Fe precipitation and redissolution. Indeed, simulations indicate that at -15 mA cm$^{-2}_{geo}$, the local pH at the interface between the Fe-N-C layer and the electrolyte solution is approximately 1.5 (**Figure 5**e). There is then a substantial and rapid increase in pH moving into the bulk catalyst layer (far from the liquid electrolyte), reaching pH values *ca*. 8-9. Consequently, only the region of the catalyst layer near the solution contributes to O_2 reduction. These conditions on the Fe Pourbaix diagram are depicted in **Figure 5**f. For the parameter values considered, >90% of the Fe-N-C layer experiences pH > 2.4, which would result in formation of Fe_2O_3 at ~0.7 V_{SHE}. Pourbaix diagrams are dependent on temperature and concentration of species. While it appears [Fe] is in order of 10^{-6} M, the Pourbaix diagram for [Fe] = 10^{-8} M at 25 $^{\circ}$C can be found for comparison in **Figure S21**. Additionally, Pourbaix diagrams were developed from metal surfaces rather than single atoms, where DFT-based models have instead been developed,[74] although here it is appears the Fe-N-C system is sufficiently represented by the Pourbaix diagram of an Fe surface.[78]
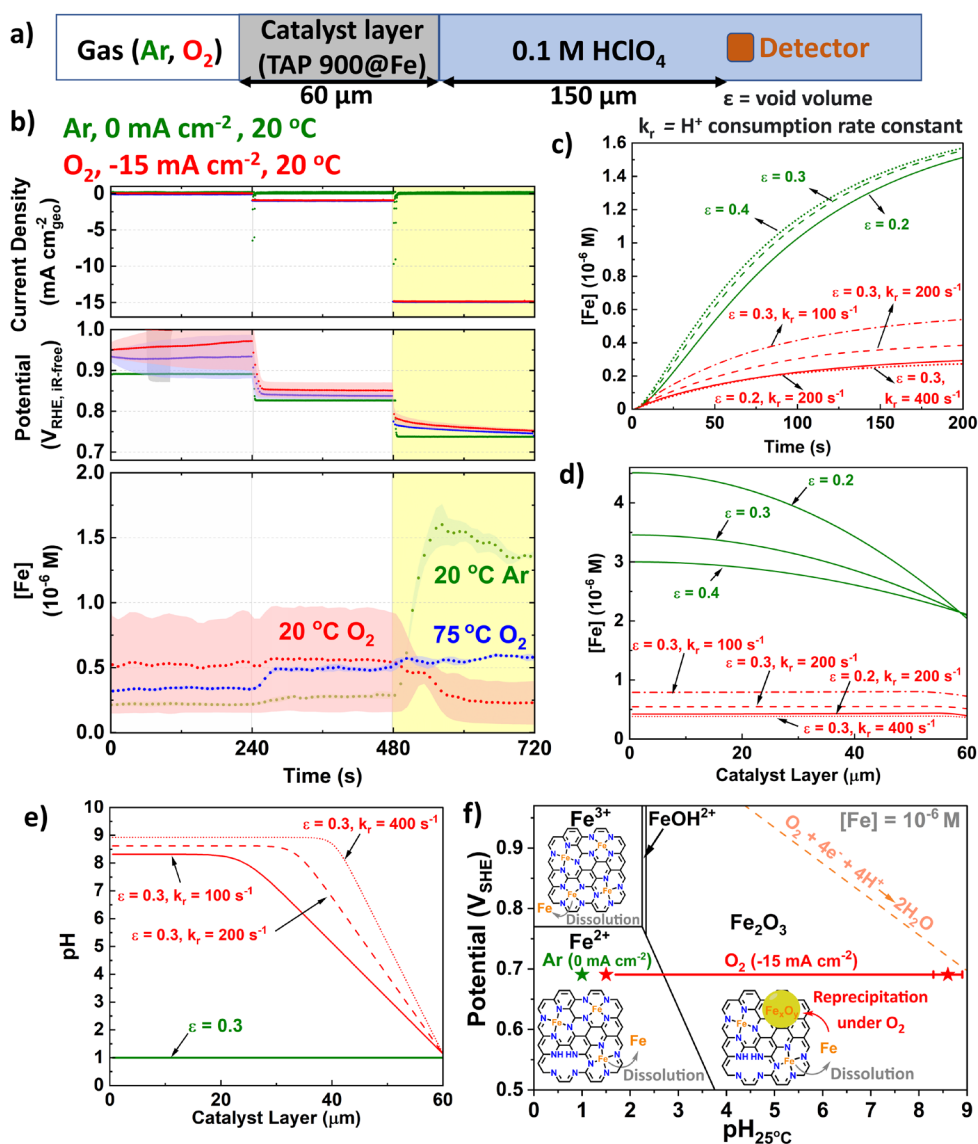
Figure 5. a.) Schematic depicting kinetically modelled system. b.) Initial GDE-ICP-MS data in terms of [Fe]. Simulated Fe concentration over c.) Time and d.) Catalyst Layer. e.) pH distribution across catalyst layer. k_r is the proton consumption rate constant and ε is the void volume. f.) Pourbaix diagram of Fe surface at 25 °C and [Fe] = 10^{-6} M with labelled points under O_2 (-15 mA cm$^{-2}_{geo}$) and Ar (0 mA cm$^{-2}_{geo}$) conditions. The error bar for O_2 represents variation of pH from different ε and k_r in Figure 5c. Fe Pourbaix diagram replotted from reference.[78]

Conclusions

Online flow cell and GDE ICP-MS setup monitored the Fe concentration profile of an Fe-N-C under inert (Ar) or active (O_2) conditions in 0.1 M $HClO_4$, with temperature effects (20 and 75 ^{o}C) investigated in online GDE ICP-MS. A microkinetic model adequately represented experimental conditions in the GDE ICP-MS system with 60 μm Fe-N-C catalyst layer at 20 ^{o}C in Ar and O_2 (at -15 mA cm^{-2}_{geo}). The model demonstrated a significant pH increase within the Fe-N-C layer under O_2 at -15 mA cm^{-2}_{geo}, leading to the formation of Fe_xO_y species, as confirmed from *post-mortem* characterization. Enhanced mass transport at 75 ^{o}C under O_2 supply resulted in higher Fe concentration detected by GDE ICP-MS and no observation of Fe_xO_y *post-mortem*. Future work will explore further kinetic modelling of the 75 ^{o}C system. We propose that increased Fe concentration under both Ar- and O_2-saturated conditions in flow cell ICP-MS arises from a lack of pH change from the limited current density (~-1 mA cm^{-2}_{geo}) and therefore, low H^+ consumption. The pH change derived from online GDE ICP-MS provides the following insights:

1. The fate of Fe (and other metal species) can vary through the catalyst layer and should be considered when conducting *operando* and *post-mortem* studies.

2. Precious metal-free layers in PEMFCs, which typically employ 60-100 $μm_{M-N-C}$ thick cathodes,[7] may not utilize the majority of the catalyst layer during O_2 reduction due to proton consumption. Focus, therefore, should be made on decreasing the electrode thickness by further increasing the electrochemically accessible volumetric active site density of precious metal-free catalysts.

Acknowledgements

References

1   F. Luo, A. Roy, M. T. Sougrati, A. Khan, D. A. Cullen, X. Wang, M. Primbs, A. Zitolo, F. Jaouen and P. Strasser, *J. Am. Chem. Soc.*, 2023, **145**, 14737–14747.

2   X. Xie, C. He, B. Li, Y. He, D. A. Cullen, E. C. Wegener, A. J. Kropf, U. Martinez, Y. Cheng, M. H. Engelhard, M. E. Bowden, M. Song, T. Lemmon, X. S. Li, Z. Nie, J. Liu, D. J. Myers, P. Zelenay, G. Wang, G. Wu, V. Ramani and Y. Shao, *Nat. Catal.*, 2020, **3**, 1044–1054.

3   M. Chen, X. Li, F. Yang, B. Li, T. Stracensky, S. Karakalos, S. Mukerjee, Q. Jia, D. Su, G. Wang, G. Wu and H. Xu, *ACS Catal.*, 2020, **10**, 10523–10534.

4   F. Luo, A. Roy, L. Silvioli, D. A. Cullen, A. Zitolo, M. T. Sougrati, I. C. Oguz, T. Mineva, D. Teschner, S. Wagner, J. Wen, F. Dionigi, U. I. Kramm, J. Rossmeisl, F. Jaouen and P. Strasser, *Nat. Mater.*, 2020, **19**, 1215–1223.

5   L. Jiao, J. Li, L. L. Richard, Q. Sun, T. Stracensky, E. Liu, M. T. Sougrati, Z. Zhao, F. Yang, S. Zhong, H. Xu, S. Mukerjee, Y. Huang, D. A. Cullen, J. H. Park, M. Ferrandon, D. J. Myers, F. Jaouen and Q. Jia, *Nat. Mater.*, 2021, **20**, 1385–1391.

6   S. Liu, C. Li, M. J. Zachman, Y. Zeng, H. Yu, B. Li, M. Wang, J. Braaten, J. Liu, H. M. Meyer, M. Lucero, A. J. Kropf, E. E. Alp, Q. Gong, Q. Shi, Z. Feng, H. Xu, G. Wang, D. J. Myers, J. Xie, D. A. Cullen, S. Litster and G. Wu, *Nat. Energy*, 2022, **7**, 652–663.

7   D. Banham, J. Y. Choi, T. Kishimoto and S. Ye, *Adv. Mater.*, 2019, **31**, 1–6.

8   H. A. Gasteiger, S. S. Kocha, B. Sompalli and F. T. Wagner, *Appl. Catal. B Environ.*, 2005, **56**, 9–35.

9   A. Mehmood, M. Gong, F. Jaouen, A. Roy, A. Zitolo, A. Khan, M. Sougrati, M. Primbs, A. M. Bonastre, D. Fongalland, G. Drazic, P. Strasser and A. Kucernak, *Nat. Catal.*, 2022, **5**, 311–323.

10   F. Jaouen, D. Jones, N. Coutard, V. Artero, P. Strasser and A. Kucernak, *Johns. Matthey Technol. Rev.*, 2018, **62**, 231–255.

11   S. T. Thompson and D. Papageorgopoulos, *Nat. Catal.*, 2019, **2**, 558–561.

12   A. Pedersen, J. Pandya, G. Leonzio, A. Serov, A. Bernardi, I. Stephens, M.-M. Titirici, C. Petit and B. Chachuat, *Green Chem.*, 2023, **25**, 10458–10471.

13   A. Pedersen, A. Bagger, J. Barrio, F. Maillard, I. Stephens and M.-M. Titirici, *J. Mater. Chem. A*, 2023, **11**, 23211–23222.

14   K. Kumar, P. Gairola, M. Lions, N. Ranjbar-Sahraie, M. Mermoux, L. Dubau, A. Zitolo, F. Jaouen and F. Maillard, *ACS Catal.*, 2018, **8**, 11264–11276.

15   Y. Zeng, C. Li, B. Li, J. Liang, M. J. Zachman, D. A. Cullen, R. P. Hermann, E. E. Alp, B. Lavina, S. Karakalos, M. Lucero, B. Zhang, M. Wang, Z. Feng, G. Wang, J. Xie, D. J. Myers, J.-P. Dodelet and G. Wu, *Nat. Catal.*, 2023, **6**, 1215–1227.

16   US DOE - Hydrogen and Fuel Cell Technologies Office, *Hydrogen and Fuel Cell Technologies Office Multi-Year Research, Development, and Demonstration Plan. Section 3.4: Fuel Cells*, 2017.

17   K. Kumar, L. Dubau, F. Jaouen and F. Maillard, *Chem. Rev.*, 2023, **123**, 9265–9326.

18   C. H. Choi, C. Baldizzone, J.-P. Grote, A. K. Schuppert, F. Jaouen and K. J. J. Mayrhofer, *Angew. Chem. Int. Ed.*, 2015, **54**, 12753–12757.

19   X. Tan, H. A. Tahini and S. C. Smith, *J. Mater. Chem. A*, 2021, **9**, 8721–8729.

20   J. Herranz, F. Jaouen, M. Lefèvre, U. I. Kramm, E. Proietti, J. P. Dodelet, P. Bogdanoff, S. Fiechter, I. Abs-Wurmbach, P. Bertrand, T. M. Arruda and S. Mukerjee, *J. Phys. Chem. C*, 2011, **115**, 16087–16097.

21   K. Kumar, T. Asset, X. Li, Y. Liu, X. Yan, Y. Chen, M. Mermoux, X. Pan, P. Atanassov, F. Maillard and L. Dubau, *ACS Catal.*, 2021, **11**, 484–494.

22   R. Chenitz, U. I. Kramm, M. Lefèvre, V. Glibin, G. Zhang, S. Sun and J.-P. Dodelet, *Energy Environ. Sci.*, 2018, **11**, 365–382.

23   C. H. Choi, H. K. Lim, M. W. Chung, G. Chon, N. Ranjbar Sahraie, A. Altin, M. T. Sougrati, L. Stievano, H. S. Oh, E. S. Park, F. Luo, P. Strasser, G. Dražić, K. J. J. Mayrhofer, H. Kim and F. Jaouen, *Energy Environ. Sci.*, 2018, **11**, 3176–3182.

24   S. Ünsal, R. Girod, C. Appel, D. Karpov, M. Mermoux, F. Maillard, V. A. Saveleva, V. Tileli, T. J. Schmidt and J. Herranz, *J. Am. Chem. Soc.*, 2023, **145**, 7845–7858.

25   G. Bae, M. M. Kim, M. H. Han, J. Cho, D. H. Kim, M.-T. Sougrati, J. Kim, K.-S. Lee, S. H. Joo, W. A. Goddard, H.-S. Oh, H. Kim, F. Jaouen and C. H. Choi, *Nat. Catal.*, 2023, 1–11.

26   C. H. Choi, C. Baldizzone, G. Polymeros, E. Pizzutilo, O. Kasian, A. K. Schuppert, N. Ranjbar Sahraie, M.-T. Sougrati, K. J. J. Mayrhofer and F. Jaouen, *ACS Catal.*, 2016, **6**, 3136–3146.

27   P. Boldrin, D. Malko, A. Mehmood, U. I. Kramm, S. Wagner, S. Paul, N. Weidler and A. Kucernak, *Appl. Catal. B Environ.*, 2021, **292**, 120169.

28   Y. Shao, J. Dodelet, G. Wu and P. Zelenay, *Adv. Mater.*, 2019, **31**, 1807615.

29   H. Zhang, L. Osmieri, J. H. Park, H. T. Chung, D. A. Cullen, K. C. Neyerlin, D. J. Myers and P. Zelenay, *Nat. Catal.*, 2022, 571–592.

30   M. Ferrandon, X. Wang, A. J. Kropf, D. J. Myers, G. Wu, C. M. Johnston and P. Zelenay, *Electrochimica Acta*, 2013, **110**, 282–291.

31   S. Liu, Q. Meyer, C. Jia, S. Wang, C. Rong, Y. Nie and C. Zhao, *Energy Environ. Sci.*, 2023, **16**, 3792–3802.

32   P. G. Santori, F. D. Speck, J. Li, A. Zitolo, Q. Jia, S. Mukerjee, S. Cherevko and F. Jaouen, *J. Electrochem. Soc.*, 2019, **166**, F3311–F3320.

33   P. P. Lopes, *ACS Mater. Au*, 2023, **3**, 8–17.

34   K. Ehelebe, J. Knöppel, M. Bierling, B. Mayerhöfer, T. Böhm, N. Kulyk, S. Thiele, K. J. J. Mayrhofer and S. Cherevko, *Angew. Chem. - Int. Ed.*, 2021, **60**, 8882–8888.

35   F. R. Nikkuni, B. Vion-Dury, L. Dubau, F. Maillard, E. A. Ticianelli and M. Chatenet, *Appl. Catal. B Environ.*, 2014, **156–157**, 301–306.

36   K. Kumar, L. Dubau, M. Mermoux, J. Li, A. Zitolo, J. Nelayah, F. Jaouen and F. Maillard, *Angew. Chem. Int. Ed.*, 2020, **59**, 3235–3243.

37   J. Li, M. T. Sougrati, A. Zitolo, J. M. Ablett, I. C. Oğuz, T. Mineva, I. Matanovic, P. Atanassov, Y. Huang, I. Zenyuk, A. Di Cicco, K. Kumar, L. Dubau, F. Maillard, G. Dražić and F. Jaouen, *Nat. Catal.*, 2021, **4**, 10–19.

38   V. Goellner, C. Baldizzone, A. Schuppert, M. T. Sougrati, K. Mayrhofer and F. Jaouen, *Phys. Chem. Chem. Phys.*, 2014, **16**, 18454–18462.

39   L. Osmieri, D. A. Cullen, H. T. Chung, R. K. Ahluwalia and K. C. Neyerlin, *Nano Energy*, 2020, **78**, 105209.

40   K. T. Santos, K. Kumar, L. Dubau, H. Ge, S. Berthon-Fabry, C. S. A. Vasconcellos, F. H. B. Lima, T. Asset, P. Atanassov, V. A. Saveleva, P. Glatzel, X. Li, F. Jaouen and F. Maillard, *J. Power Sources*, 2023, **564**, 232829.

41   V. A. Saveleva, K. Kumar, P. Theis, N. S. Salas, U. I. Kramm, F. Jaouen, F. Maillard and P. Glatzel, *ACS Appl. Energy Mater.*, 2023, **6**, 611–616.

42   J. Barrio, A. Pedersen, S. Ch. Sarma, A. Bagger, M. Gong, S. Favero, C. Zhao, R. Garcia-Serres, A. Y. Li, Q. Zhang, F. Jaouen, F. Maillard, A. Kucernak, I. E. L. Stephens and M. Titirici, *Adv. Mater.*, 2023, **35**, 2211022.

43   M. Primbs, Y. Sun, A. Roy, D. Malko, A. Mehmood, M.-T. Sougrati, P.-Y. Blanchard, G. Granozzi, T. Kosmala, G. Daniel, P. Atanassov, J. Sharman, C. Durante, A. Kucernak, D. Jones, F. Jaouen and P. Strasser, *Energy Environ. Sci.*, 2020, **13**, 2480–2500.

44   X. Wan, X. Liu, Y. Li, R. Yu, L. Zheng, W. Yan, H. Wang, M. Xu and J. Shui, *Nat. Catal.*, 2019, **2**, 259–268.

45   J.-Q. Zhong, K.-J. Yan, J. Yang, W.-H. Yang and X.-D. Yang, *ACS Catal.*, 2022, **12**, 9003–9010.

46   F. Jaouen, V. Goellner, M. Lefèvre, J. Herranz, E. Proietti and J. P. Dodelet, *Electrochimica Acta*, 2013, **87**, 619–628.

47   V. Gridin, J. Du, S. Haller, P. Theis, K. Hofmann, G. K. H. Wiberg, U. I. Kramm and M. Arenz, *Electrochimica Acta*, 2023, **444**, 142012.

48   D. Malko, A. Kucernak and T. Lopes, *Nat. Commun.*, 2016, **7**, 13285.

49   S. Rojas-Carbonell, K. Artyushkova, A. Serov, C. Santoro, I. Matanovic and P. Atanassov, *ACS Catal.*, 2018, **8**, 3041–3053.

50   M. Gong, A. Mehmood, B. Ali, K.-W. Nam and A. Kucernak, *ACS Catal.*, 2023, **13**, 6661–6674.

51   A. Bonnefont, *Curr. Opin. Electrochem.*, 2023, **39**, 1–8.

52   A. S. Varela, M. Kroschel, T. Reier and P. Strasser, *Catal. Today*, 2016, **260**, 8–13.

53   A. S. Varela, *Curr. Opin. Green Sustain. Chem.*, 2020, **26**, 100371.

54   A. Muthukrishnan and A. James, *Catal. Sci. Technol.*, 2022, **12**, 6246–6255.

55   G. Bae, M. W. Chung, S. G. Ji, F. Jaouen and C. H. Choi, *ACS Catal.*, 2020, **10**, 8485–8495.

56   M. Rouhet, S. Bozdech, A. Bonnefont and E. R. Savinova, *Electrochem. Commun.*, 2013, **33**, 111–114.

57   I. V. Zenyuk and S. Litster, *ECS Trans.*, 2013, **58**, 27–35.

58   F. Jaouen, M. Lefèvre, J.-P. Dodelet and M. Cai, *J. Phys. Chem. B*, 2006, **110**, 5553–5558.

59   J.-Y. Choi, L. Yang, T. Kishimoto, X. Fu, S. Ye, Z. Chen and D. Banham, *Energy Environ. Sci.*, 2017, **10**, 296–305.

60   X. Yin and P. Zelenay, *ECS Trans.*, 2018, **85**, 1239.

61   G. Zhang, X. Yang, M. Dubois, M. Herraiz, R. Chenitz, M. Lefèvre, M. Cherif, F. Vidal, V. P. Glibin, S. Sun and J.-P. Dodelet, *Energy Environ. Sci.*, 2019, **12**, 3015–3037.

62   J.-P. Dodelet, V. Glibin, G. Zhang, U. I. Kramm, R. Chenitz, F. Vidal, S. Sun and M. Dubois, *Energy Environ. Sci.*, 2021, **14**, 1034–1041.

63   X. Yin, E. F. Holby and P. Zelenay, *Energy Environ. Sci.*, 2021, **14**, 1029–1033.

64   K. Ehelebe, D. Seeberger, M. T. Y. Paul, S. Thiele, K. J. J. Mayrhofer and S. Cherevko, *J. Electrochem. Soc.*, 2019, **166**, F1259.

65   Y.-P. Ku, K. Ehelebe, A. Hutzler, M. Bierling, T. Böhm, A. Zitolo, M. Vorokhta, N. Bibent, F. D. Speck, D. Seeberger, I. Khalakhan, K. J. J. Mayrhofer, S. Thiele, F. Jaouen and S. Cherevko, *J. Am. Chem. Soc.*, 2022, **144**, 9753–9763.

66   K. H. Gayer and L. Woontner, *J. Phys. Chem.*, 1956, **60**, 1569–1571.

67   M. Pourbaix, *Atlas of Electrochemical Equilibria in Aqueous Solutions*, National Association of Corrosion Engineers, 1974.

68   K. Ebner, L. Ni, V. A. Saveleva, B. P. L. Monnier, A. H. Clark, F. Krumeich, M. Nachtegaal, J. S. Luterbacher, U. I. Kramm, T. J. Schmidt and J. Herranz, *Phys. Chem. Chem. Phys.*, 2021, **23**, 9147–9157.

69   S. C. Sarma, J. Barrio, A. Bagger, A. Pedersen, M. Gong, H. Luo, M. Wang, S. Favero, C. Zhao, Q. Zhang, A. Kucernak, M. Titirici and I. E. L. Stephens, *Adv. Funct. Mater.*, 2023, 2302468.

70   N. Ramaswamy, U. Tylus, Q. Jia and S. Mukerjee, *J. Am. Chem. Soc.*, 2013, **135**, 15443–15449.

71   X. Wang, M. Ferrandon, J. H. Park, J.-J. Shen, A. J. Kropf, H. Zhang, P. Zelenay and D. J. Myers, *Electrochimica Acta*, 2023, **443**, 141934.

72   U. A. Paulus, T. J. Schmidt, H. A. Gasteiger and R. J. Behm, *J. Electroanal. Chem.*, 2001, **495**, 134–145.

73   M. N. Jackson, O. Jung, H. C. Lamotte and Y. Surendranath, *ACS Catal.*, 2019, **9**, 3737–3743.

74   E. F. Holby, G. Wang and P. Zelenay, *ACS Catal.*, 2020, **10**, 14527–14539.

75   K. C. Neyerlin, W. Gu, J. Jorne and H. A. Gasteiger, *J. Electrochem. Soc.*, 2006, **153**, A1955.

76   S. Komini Babu, H. T. Chung, P. Zelenay and S. Litster, *ACS Appl. Mater. Interfaces*, 2016, **8**, 32764–32777.

77   S. J. Ridge, R. E. White, Y. Tsou, R. N. Beaver and G. A. Eisman, *J. Electrochem. Soc.*, 1989, **136**, 1902.

78   B. Beverskog and I. Puigdomenech, *Corros. Sci.*, 1996, **38**, 2121–2135.